Microelectronic Engineering 276 (2023) 112008

Contents lists available at ScienceDirect

Microelectronic Engineering

journal homepage: www.elsevier.com/locate/mee

Variability and power enhancement of current controlled resistive switching devices

G. Vinuesa [a,*], H. García [a], J.M. Lendínez [a], E. García-Ochoa [a], M.B. González [b], D. Maldonado [c], C. Aguilera-Pedregosa [c], E. Moreno [c], F. Jiménez-Molinos [c], J.B. Roldán [c], F. Campabadal [b], H. Castán [a], S. Dueñas [a]

[a] Departamento de Electrónica, Universidad de Valladolid, Paseo Belén 15, 47011 Valladolid, Spain
[b] Institut de Microelectrònica de Barcelona IMB-CNM (CSIC), Campus UAB, Carrer dels Til·lers s/n, Campus UAB, 08193 Bellaterra, Spain
[c] Departamento de Electrónica y Tecnología de Computadores, Universidad de Granada, Facultad de Ciencias, Avd. Fuentenueva s/n, 18071 Granada, Spain

ARTICLE INFO

Keywords:
Resistive switching
Hafnium oxide
Current control
Electrical characterization
TCM
RRAM

ABSTRACT

In this work, the unipolar resistive switching behaviour of Ni/HfO_2/Si(n^+) devices is studied. The structures are characterized using both current and voltage sweeps, with the device resistance and its cycle-to-cycle variability being analysed in each case. Experimental measurements indicate a clear improvement on resistance states stability when using current sweeps to induce both set and reset processes. Moreover, it has been found that using current to induce these transitions is more efficient than using voltage sweeps, as seen when analysing the device power consumption. The same results are obtained for devices with a Ni top electrode and a bilayer or pentalayer of HfO_2/Al_2O_3 as dielectric. Finally, kinetic Monte Carlo and compact modelling simulation studies are performed to shed light on the experimental results.

1. Introduction

In the last few years, several emerging technologies for non-volatile memories are being studied to work as storage-class memories [1]. Among these technologies, resistive random-access memories (RRAMs) based on the resistive switching (RS) effect are of great interest [2–4]. Their outstanding features allow to bridge the gap between flash memories and the low latency dynamical memories. RRAMs have shown great potential for scalability, high-speed operation (<10 ns), low power consumption and CMOS compatibility [5–7]. In addition, they also show remarkable endurance (above $>10^{10}$ cycles [8]), retention [9–11] and large HRS/LRS resistance ratios (>100) [1]. This technology is being used by different companies commercially, such as TSMC for its 40 nm [12], 28 nm [13] and 22 nm [14] nodes, and INTEL for its 22 nm [15] node. Moreover, RS devices are not only key elements for non-volatile memories [1], but have also proven outstanding properties for applications such as hardware cryptography [16–18] and neuromorphic computation [9,16,19].

As stated before, RRAMs are based on the resistive switching (RS) effect, which allows the devices to reversibly change their electrical resistance by applying a certain electric field [9]. The programmed resistance value remains without the application of any external voltage, which is what makes these devices good candidates for non-volatile memories. As RRAM devices are usually metal-insulator-metal or metal-insulator-(highly doped) semiconductor structures, this change in the device's resistance is explained by the modification of an energy barrier at one of the dielectric/electrode interfaces or by the formation of a conductive filament (CF) that short-circuits the electrodes [20–22]. Filamentary charge conduction linked to CF formation is the most common RS operation; the CF is created for the first time in the forming process (for forming-free devices this stage is not necessary), which demands higher voltages than the subsequent switching processes. After the forming, the filament can be disrupted (reset process) and rebuilt (set process) repeatedly, switching the device resistance state from high (HRS) to low (LRS) or vice versa, respectively. In addition, intermediate states are also allowed and controllable in some switching devices, which makes them specially interesting for the implementation of artificial synapses in neuromorphic computation, as this multilevel operation allows to electrically adjust the synaptic weight between neurons [23,24]. This filamentary model is widely accepted by the scientific community [7,25–27] and has been experimentally demonstrated in several previous works [20,28–30].

* Corresponding author.
E-mail address: guillermo.vinuesa@uva.es (G. Vinuesa).

https://doi.org/10.1016/j.mee.2023.112008
Received 21 February 2023; Received in revised form 5 April 2023; Accepted 14 April 2023
Available online 15 April 2023
0167-9317/© 2023 The Authors. Published by Elsevier B.V. This is an open access article under the CC BY license (http://creativecommons.org/licenses/by/4.0/).

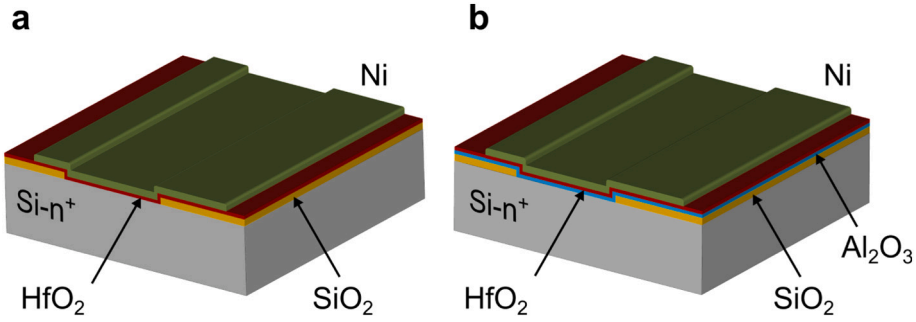

Fig. 1. Schematic cross-sections of the fabricated **a** Ni/HfO_2/Si-n^+ and **b** Ni/HfO_2/Al_2O_3/Si-n^+ devices.

Resistive switching can either be bipolar (BRS) if the set and reset occur at different polarities or unipolar (URS) when both transitions happen at the same voltage polarity. When the electrodes are inert metals, the BRS is usually due to electron hopping through dielectric regions with a high concentration of oxygen vacancies, which shape the conductive filaments (known as valence change mechanism or VCM [10,31,32]). However, if one of the electrodes is an electrochemically active metal (Ag, Cu or Ni), it may act as a source of highly mobile metal cations that may diffuse through the insulator, forming a metallic filament (electrochemical metallization mechanism or ECM) [2,27,33].

Thermal effects are known to play a key role to analyse RS in RRAMs [2,9,10,34]. They are particularly important in some types of URS devices, as they are based on the thermochemical mechanism (TCM), in which thermochemical processes dominate over the electrochemical ones [35–39]. It has been shown for URS devices with Ag electrodes [40–42], as well as for Ni/HfO_2/Si-n^+ samples [33,43–46] that Joule heating is key to explain the physics that lies behind RS operation.

As stated earlier, RRAMs are serious candidates to replace other technologies in the non-volatile memory realm. However, the cycle-to-cycle (C2C) variability hinders their progress to become the mainstream technology in the industry. This is especially apparent in unipolar resistive switching devices, which has led to a decrease in the number of scientific studies of samples presenting URS [47], despite the fact that they usually show much greater low to high resistance state ratio and easier circuit integration (because of their unipolar nature) when compared to their bipolar counterparts [48]. In this context, different alternatives have been explored to assess the potential of these devices; for instance, the use of the device current instead of the voltage to control RS operation. The use of the current to induce RS allows a better control of the device resistance in HfO_2-based RRAM devices, especially in the set process [49,50]. We deal with this current-driven RS approach here to characterize Ni/HfO_2/Si-n^+ cells from the experimental and simulation viewpoint. In addition, we consider Ni/HfO_2/Al_2O_3/Si-n^+ and Ni/HfO_2/Al_2O_3/HfO_2/Al_2O_3/HfO_2/Si-n^+ structures to extend our study since the presence of the alumina layer in the dielectric stack modifies the thermal effects [51] and allows to thermal engineer the dielectric stacks to improve RS operation. To shed light on these issues, the set and reset voltages, the power consumption at RS transitions, and the variability and thermal effects are studied in depth comparing current and voltage-controlled resistive switching and the physics behind RS by means of COMSOL-based simulations.

2. Material and methods

Ni/insulator/Si stacks were fabricated on (100) n-type Czochralski silicon wafers with resistivity in the (0.007–0.013) Ω cm range. Both HfO_2 and Al_2O_3 layers were grown at 225 °C using Atomic Layer Deposition in a Cambridge NanoTech Savannah 200 system equipped with tetrakis(dimethylamido)-hafnium (TDMAH) and trimethylaluminum (TMA) as Hf and Al precursors, respectively, H_2O as oxidant precursor and N_2 as carrier and purge gas. Three different types of devices are studied in the present work, namely a monolayer Ni/HfO_2(20 nm)/Si-n^+, a bilayer Ni/HfO_2(10 nm)/Al_2O_3(10 nm)/Si-n^+ and a pentalayer Ni/HfO_2(4 nm)/Al_2O_3(4 nm)/HfO_2(4 nm)/Al_2O_3(4 nm)/HfO_2(4 nm)/Si-n^+. The 200 nm thick Ni electrode was deposited by magnetron sputtering. The resulting devices are squared cells of 60 × 60 μm^2. All fabrication details have been published and can be found at [51]. A schematic cross-section of the devices can be found in Fig. 1.

Electrical measurements were made by means of a HP4155B semiconductor parameter analyzer. Voltage and current sweeps were applied to the top electrode (TE) of the devices, while the bottom electrode (BE) remained grounded in all cases. Current and voltage compliances were used when inducing a set process by applying voltage, or a reset process applying current, respectively. After each transition, a pulse at 0.5 V was applied to the device to measure the current at a low voltage and ensure that the transition had been completed by checking whether this value was over or under a current limit (I_{lim}) obtained experimentally. The automated measuring process is further detailed on a flowchart in Fig. 2. The equipment was connected to a computer via GPIB and controlled using Agilent VEE software.

3. Results and discussion

3.1. Experimental approach

After an electroforming process carried out by applying a positive voltage ramp and using a current compliance of 100 μA, Ni/HfO_2/Si-n^+ devices showed unipolar resistive switching. Thus, both set and reset processes take place at a positive voltage polarity, with the set process occurring at higher voltages but consuming less power (because of the higher currents involved in the reset). The typical current-voltage (I-V) curves are shown in Fig. 3a, obtained under ramped voltage stress (RVS), the set was observed in a [1.8 V, 2.5 V] voltage interval, while the reset occurred in the [1.2 V, 2 V] range. A current compliance of 1 mA was used for the set transition to avoid irreversibly breaking the sample. As stated in the introduction section, the URS in these samples is driven by Joule heating inducing both the formation and rupture of CFs; high mobility Ni atoms diffuse from the top electrode into the dielectric creating a metallic conductive path [43,52]. The I-V curve is obtained by measuring the current through the device while applying a voltage bias. This is the usual characterization technique for both bi- and unipolar RS devices. As the aim of this work is to uncover the consequences and possible benefits of current controlled RS, we obtained a very similar hysteretic curve by applying ramped current stress (RCS) and measuring the voltage across the device (with a voltage compliance of 2 V). We shall call this a voltage-current V-I curve, which is depicted in Fig. 3b.

Hereby we present an analysis of the charge, flux and energy, as these magnitudes control de Joule heating, which, as mentioned in the introduction, is essential for URS. Charge versus flux (Q-ϕ) and energy versus flux (*E*-ϕ) curves are plotted in Fig. 4 a-b for the reset cycles obtained under RVS (see Eqs. 1–3). The charge can be calculated from the conventional I-V curves as follows:

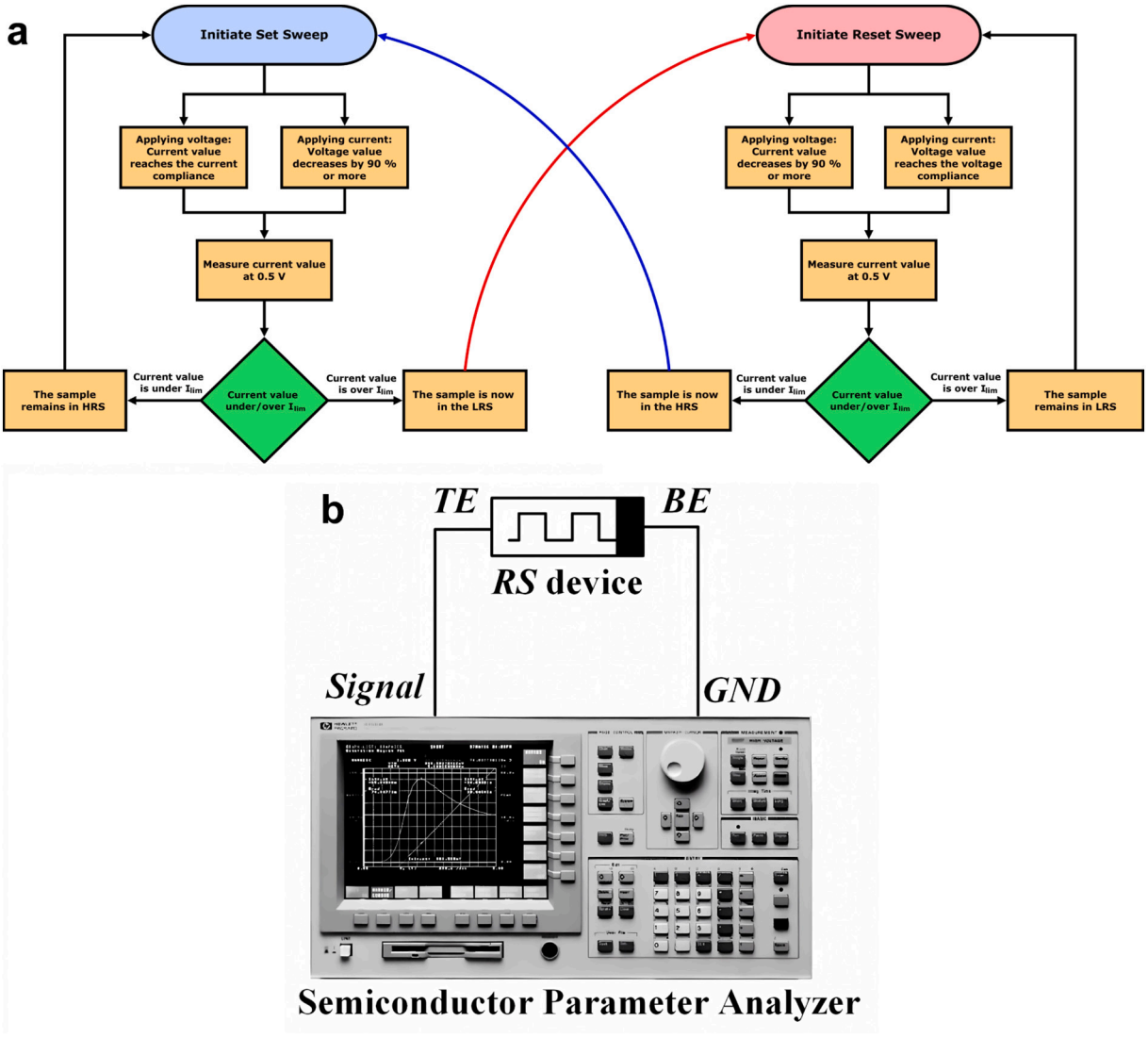

Fig. 2. **a** Schematic of the automated measuring process of the Ni/HfO_2/Si-n^+ devices. The algorithm shows the necessary conditions to ensure that the transition has been completed for both voltage and current sweeps. **b** Schematic of the circuit used for the electrical measurements, the HP4155B semiconductor parameter analyzer allows for the application of voltage and current via its Source Measure Units (SMUs). TE and BE stand for top electrode and bottom electrode, respectively.

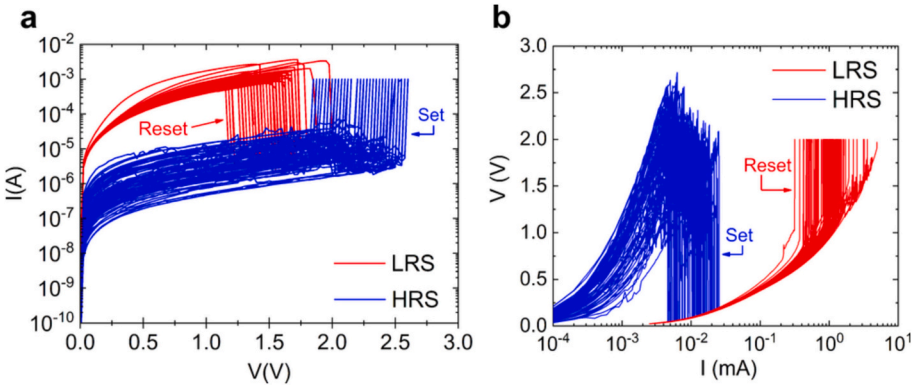

Fig. 3. Experimental **a** I-V and **b** V-I curves of a Ni/HfO_2/Si-n^+ device, LRS and reset processes are depicted in red, while HRS and set processes appear in blue. (For interpretation of the references to colour in this figure legend, the reader is referred to the web version of this article.)

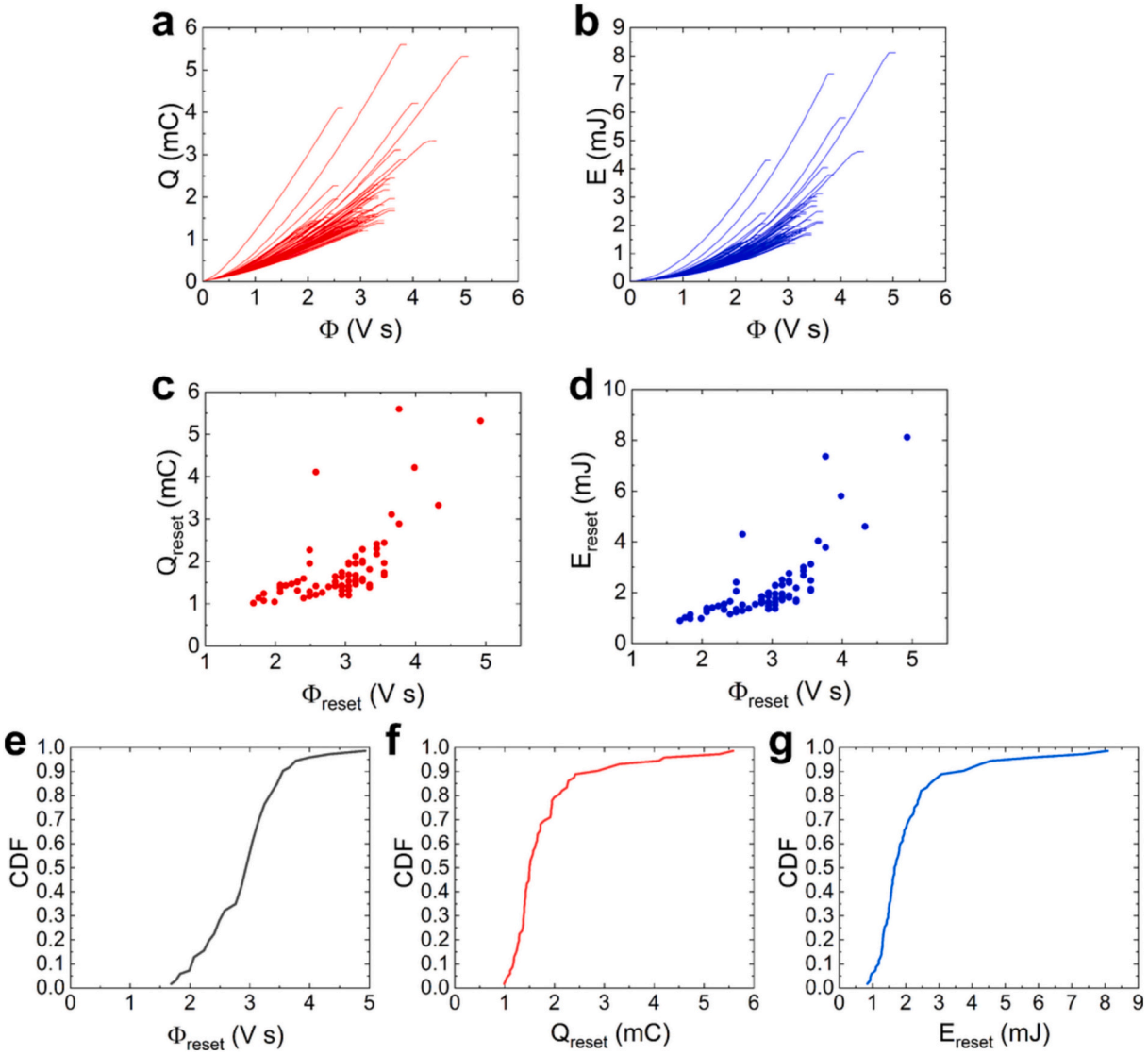

Fig. 4. **a** Charge versus flux data, **b** energy versus flux data for the Ni/HfO_2/Si-n^+ device measured under RVS (Fig. 3a). **c** Extracted charge and flux experimental data at the reset point, **d** energy versus flux at the reset point for the devices under study measured under RVS (Fig. 3a). Cumulative distribution functions for **e** ϕ_{reset}, **f** Q_{reset} and **g** E_{reset} for the devices under study measured employing RVS (Fig. 3a).

$$Q(t) = \int_0^t i(t')\,dt' \tag{1}$$

where i(t) and v(t) are the measured current and voltage. And the flux can be computed as:

$$\Phi(t) = \int_0^t v(t')\,dt' \tag{2}$$

Thus, the corresponding energy value can be derived by the equation:

$$E(t) = \int_0^t i(t')v(t')\,dt' \tag{3}$$

At the reset point, the charge, flux and energy obtained are named as Q_{reset}, ϕ_{reset} and E_{reset}. The Q_{reset} versus ϕ_{reset} experimental distributions are plotted in Fig. 4 c-d along with the E_{reset} versus ϕ_{reset} distributions for the RVS cycles. The cumulative distribution functions (CDF) for ϕ_{reset}, Q_{reset} and E_{reset}, corresponding to these experimental distributions, are shown in Fig. 4 e-g. See that the distribution functions are much more abrupt in Fig. 4f and g. These results make sense since, as stated before, these magnitudes control the Joule heating and, therefore, the CF temperature that ultimately triggers the reset process (which is known to be a thermal-run-away process with positive feedback) [34,46].

In Fig. 5a the set voltage CDFs are shown both for I-V and V-I measurements, while their corresponding set currents are presented in Fig. 5b. Lower set voltages are obtained in the V-I case, while there is no difference between the two measurement approaches in the case of the set currents. The algorithms employed to extract the set voltages in the I-V curves are given in [53]. For the V-I curves, the set voltages are found at the point where the highest voltage change is obtained. Furthermore, the same observation can be made when analysing the reset transition. Reset voltages are lower using RCS in comparison with the voltage-controlled approach (Fig. 5c); while reset currents were similar for both current and voltage measurements, as it can be seen in Fig. 5d. The algorithm used for the reset voltage extraction can also be found at [53].

To obtain significant information about the changes in the device resistance after each transition, the current was read at 0.5 V after the set or reset process (Fig. 2). This was made for both RVS and RCS using the

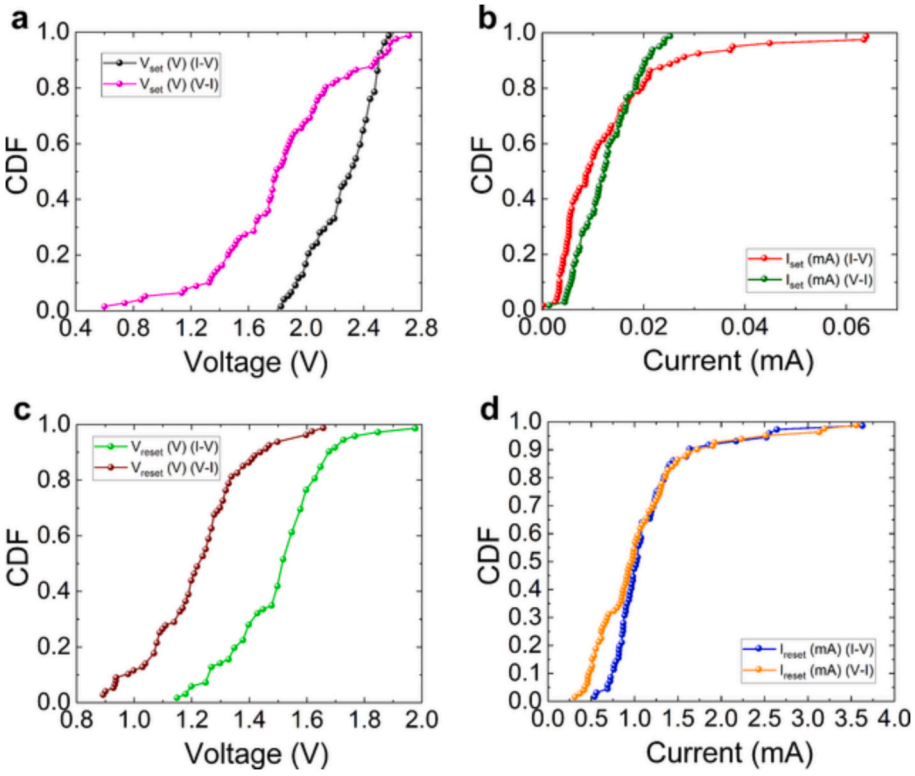

Fig. 5. Cumulative distribution functions for **a** V_{set} under RVS (black) and RCS (pink), **b** I_{set} under RVS (red) and RCS (dark green), **c** V_{reset} under RVS (light green) and RCS (maroon), and **d** I_{reset} under RVS (blue) and RCS (orange), for the Ni/HfO_2/Si-n^+ device. (For interpretation of the references to colour in this figure legend, the reader is referred to the web version of this article.)

following measurement sequence: (i) voltage or current sweep to trigger the **set** process, (ii) voltage pulse of 0.5 V to measure the current, (iii) voltage or current sweep to trigger the **reset** process, (iv) voltage pulse of 0.5 V to measure the current. Fig. 6a and b (HfO_2 monolayer) show the current measured at 0.5 V (steps (ii) and (iv)) after each set or reset transition versus the number of cycles. The resistance uniformity along cycling under RCS is notorious in comparison to RVS. Although the resistance variability in the LRS is similar for both cases, HRS variability is clearly lower in the RCS case.

In order to shed light on the variability issue, we also considered devices with more complex dielectrics such as Ni/HfO_2/Al_2O_3/Si-n^+ bilayers and Ni/HfO_2/Al_2O_3/HfO_2/ Al_2O_3/HfO_2/Si-n^+ pentalayers. We have observed a similar behaviour for the bi- (Fig. 6 c-d) and pentalayer (Fig. 6 e-f) devices in terms of the RCS advantages. Variability is lower due to uniformity in Joule heating under RCS, as thermal effects are controlled by the device current.

These observations are supported by the calculation of the standard deviation of the HRS and LRS under both RCS and RVS for the three samples, which are shown in Table 1. The standard deviations show that applying current sweeps positively impacts both resistance states' variability when compared to the results obtained by applying voltage sweeps. HRS standard deviation decreases in one order of magnitude in all cases when using RCS, also decreasing one order of magnitude for the LRS of the bilayer device. In the monolayer and pentalayer structures, the standard deviation of the LRS also decreases, although within the same order of magnitude, when using RCS. When analysing the mean values, it can be seen that the mean current value obtained decreases greatly for the HRS in all cases, while the LRS mean values remain similar under RCS and RVS.

Fig. 7 shows that the power involved in RS processes is lower for RCS than for RVS operation. These tendency holds for both set and reset transitions in all the dielectric stacks considered. Again, the efficiency in controlling Joule effects under RCS is behind the physics underlying this behaviour. This draws even more attention to the reset process, as it consumes less power while also delivering lower current values (see mean values on Table 1) under current control. Set and reset power values are obtained by multiplying current and voltage values at the point where the voltage presents a higher change in its value.

3.2. Simulation approach

A 3D finite elements approach was employed to simulate the devices under study; in particular, the Ni/HfO_2/Si-n^+ cell. The different materials and their properties were described making use of the commercial simulation software COMSOL Multiphysics. A cylindrical CF was assumed, whose radius was modified to reproduce the experimental RS processes.

In addition to the ohmic CF, we have also included a constriction within the CF that corresponds to an atomic-size narrowing, where electron transport is ballistic and quantum effects show up. The transport regime can be described with the Landauer's formalism [54–56]. Under the assumption of a transmission probability function resembling an inverted parabolic function, Landauer's integral for the zero-temperature limit can be analytically solved. The current across the constriction can be obtained as follows,

$$I = \frac{2eN}{h}\left\{eV + \frac{1}{\alpha}ln\left[\frac{1+e^{[\alpha(\Phi-\beta eV)]}}{1+e^{\{\alpha[\Phi+(1-\beta)eV]\}}}\right]\right\} \quad (4)$$

where e is the electron charge, h is the Planck's constant, N is the number of active channels in the constriction, α affects the shape of the potential barrier, Φ stands for the potential barrier height, β is the fraction of the potential that drops in one of the constriction contacts and (1- β) the

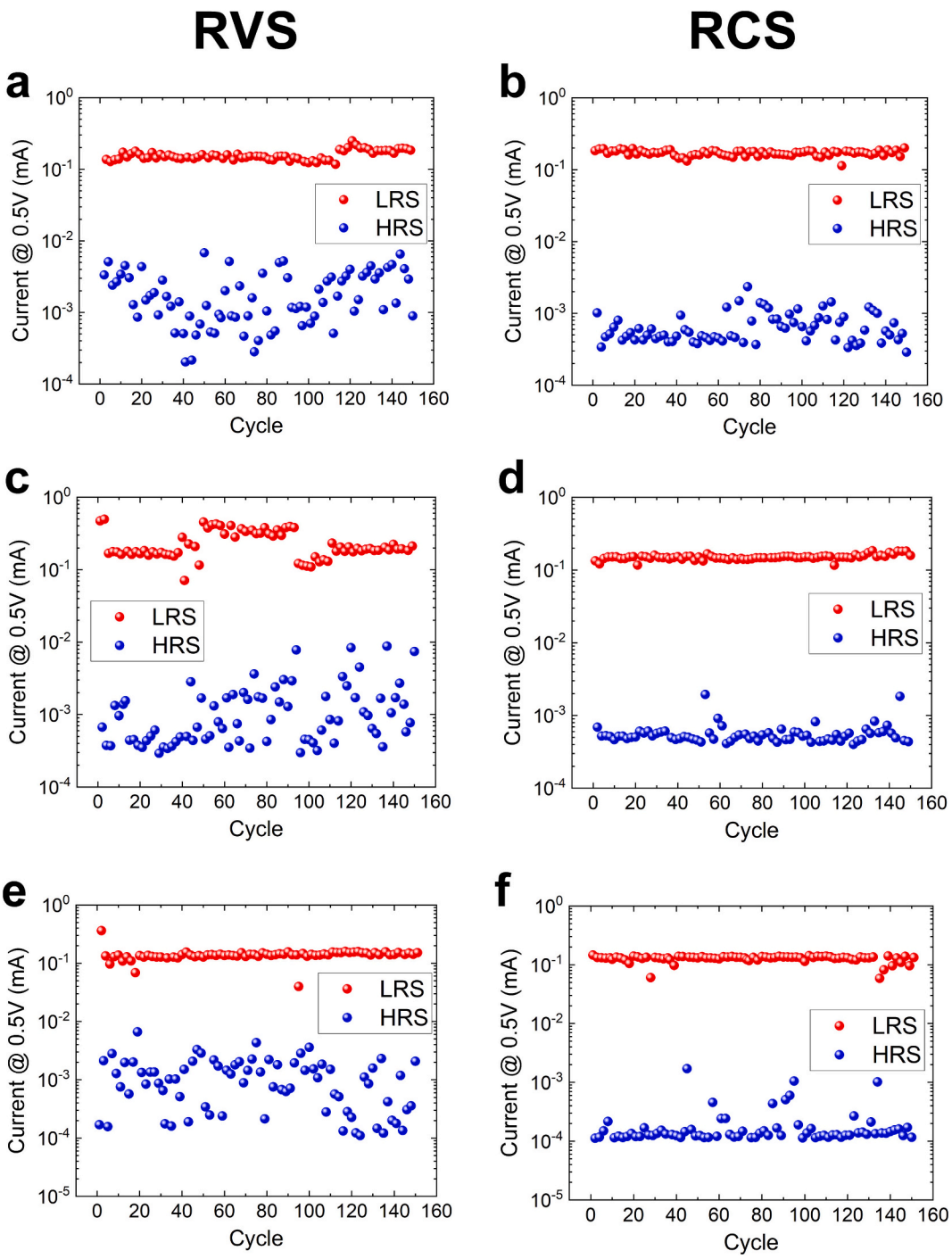

Fig. 6. Current values measured at 0.5 V after each set (LRS- red) and reset (HRS-blue) transition, carried out under RVS (left column) and RCS (right column) for the Ni/HfO_2/Si-n^+ (**a** and **b**), Ni/HfO_2/Al_2O_3/Si-n^+ (**c** and **d**) and Ni/HfO_2/Al_2O_3/HfO_2/Al_2O_3/HfO_2/Si-n^+ (**e** and **f**) samples. (For interpretation of the references to colour in this figure legend, the reader is referred to the web version of this article.)

Table 1
Standard deviation (σ) and mean (μ) values of the HRS and LRS under RVS and RCS for the three measured samples, a monolayer Ni/HfO_2(20 nm)/Si-n^+, a bilayer Ni/HfO_2(10 nm)/Al_2O_3(10 nm)/Si-n^+ and a pentalayer Ni/HfO_2(4 nm)/Al_2O_3(4 nm)/HfO_2(4 nm)/Al_2O_3(4 nm)/HfO_2(4 nm)/Si-n^+.

		HRS		LRS	
		σ (A)	μ (A)	σ (A)	μ (A)
Monolayer	**RVS**	$1.60 \bullet 10^{-6}$	$2.11 \bullet 10^{-6}$	$2.49 \bullet 10^{-5}$	$1.58 \bullet 10^{-4}$
	RCS	$3.60 \bullet 10^{-7}$	$6.79 \bullet 10^{-7}$	$1.53 \bullet 10^{-5}$	$1.70 \bullet 10^{-4}$
Bilayer	**RVS**	$1.79 \bullet 10^{-6}$	$1.47 \bullet 10^{-6}$	$1.03 \bullet 10^{-4}$	$2.36 \bullet 10^{-4}$
	RCS	$2.42 \bullet 10^{-7}$	$5.72 \bullet 10^{-7}$	$1.23 \bullet 10^{-5}$	$1.51 \bullet 10^{-4}$
Pentalayer	**RVS**	$1.11 \bullet 10^{-6}$	$1.24 \bullet 10^{-6}$	$3.19 \bullet 10^{-5}$	$1.40 \bullet 10^{-4}$
	RCS	$2.43 \bullet 10^{-7}$	$2.05 \bullet 10^{-7}$	$1.58 \bullet 10^{-5}$	$1.28 \bullet 10^{-4}$

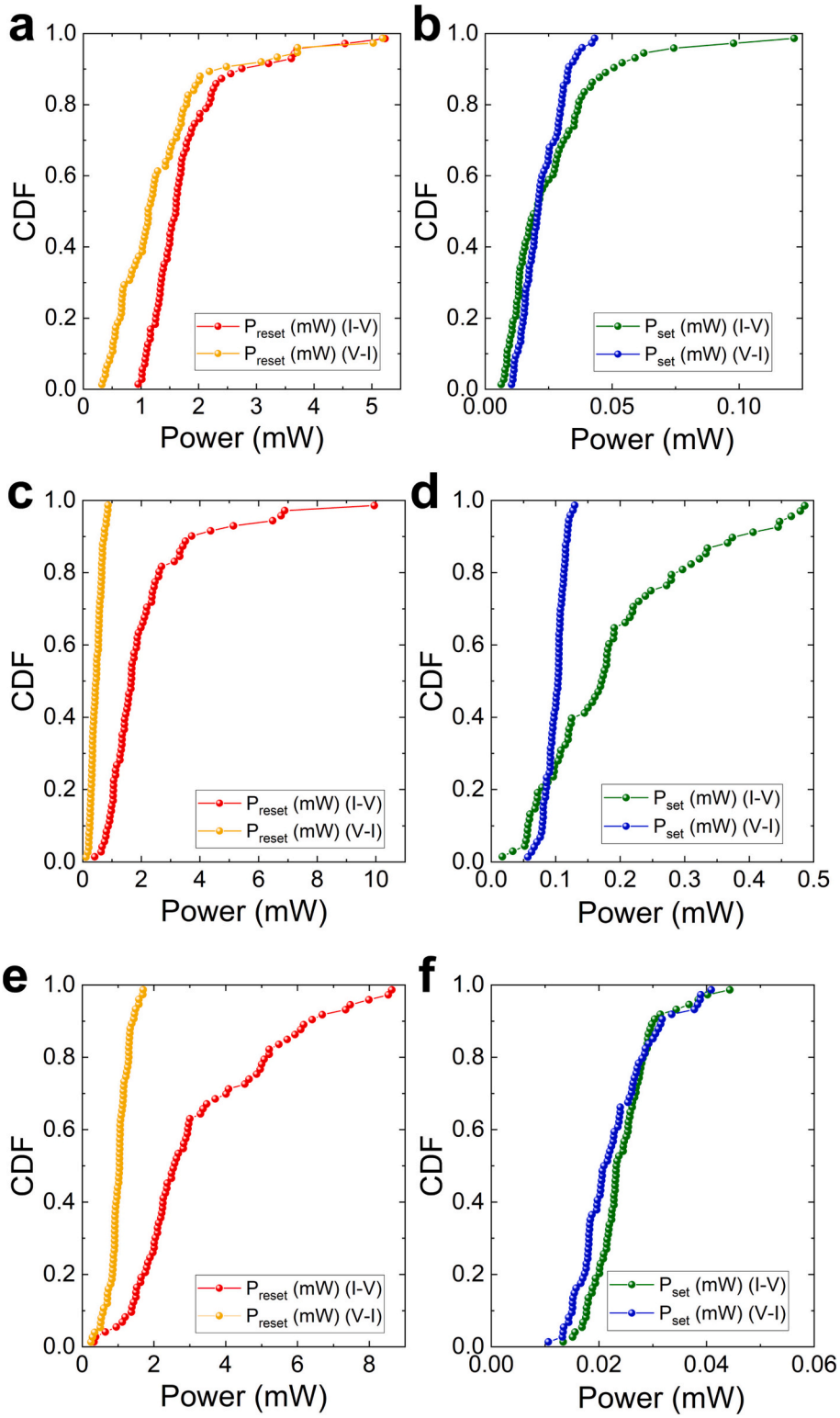

Fig. 7. Cumulative distribution functions for the power consumption for both reset (left column) and set (right column) transitions for Ni/HfO_2/Si-n^+ (**a - b**), Ni/HfO_2/Al_2O_3/Si-n^+ (**c - d**) and Ni/HfO_2/Al_2O_3/HfO_2/Al_2O_3/HfO_2/Si-n^+ (**e - f**) samples. Panels (**a, c, e)** show the power absorbed by the reset transition when applying voltage (red) and current (yellow). Panels (**b, d, f)** show the power absorbed by the set transition when applying voltage (green) and current (blue). (For interpretation of the references to colour in this figure legend, the reader is referred to the web version of this article.)

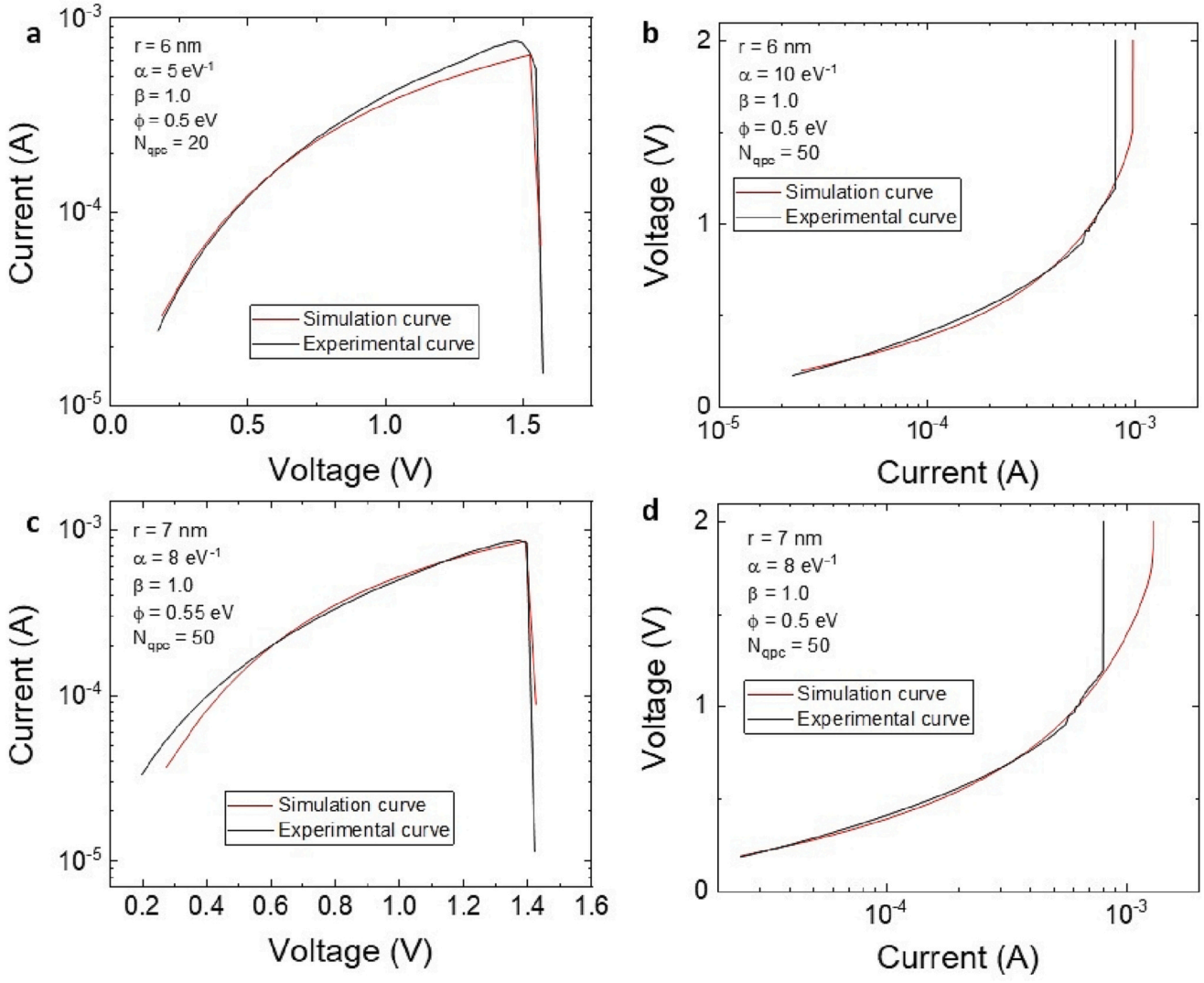

Fig. 8. Simulated (red lines) and experimental (black lines) curves for Ni/HfO_2/Si-n^+ devices. **a, c** I-V operation regime, **b, d** V-I operation regime. (For interpretation of the references to colour in this figure legend, the reader is referred to the web version of this article.)

other fraction. The simulation scheme is equivalent to the one proposed in [26,51] for the same kind of devices.

In addition, the CF radius evolution is described assuming an average Arrhenius-like mechanism to account for the variation of the high concentration regions of metallic atoms that shape the CF and lead to the set and reset processes [57].

$$\frac{dr}{dt} = \pm A\, e^{-\frac{E_a}{kT}} \tag{5}$$

where r stands for the CF radius (cylindrical coordinates), A stands for a fitting preexponential constant and E_a is the activation energy of the main physical mechanism behind the CF variation (we simplify the model under the assumption that the mechanism described in Eq. 2 has the strongest influence in the CF kinetics; a different simulation approach, accounting for the different physical mechanisms is based on kinetic Monte Carlo [33]). The CF thermal conductivity was 11 WK^{-1} m^{-1}, while it was 90 (148) WK^{-1} m^{-1} for the Ni (Silicon) electrode, and 1 WK^{-1} m^{-1} for HfO_2; the CF electrical conductivity was 2×10^5 Ω^{-1} m^{-1} and the activation energy, $E_a = 0.84$ eV.

We show in Fig. 8 that the simulation tool reproduces reasonably well the experimental measurements once the CF radius and the QPC model parameters are fitted.

See that both I-V and V-I operation regimes are correctly described, including the set and reset voltages, the current magnitude and the curves shape. This is also seen in Fig. 9, where a comparison with a group of experimental curves (note the cycle-to-cycle variability) is shown along with simulated ones.

Our scheme is in line with previous simulation approaches; however, it makes no difference when V-I and I-V operation regimes are compared since it is a deterministic simulator. To shed light on this issue, we have plotted in Fig. 10 the product of temperature and electric field versus voltage drop in the device; these two magnitudes drive ion diffusion in the dielectric and, therefore, control RS. In this respect, the plot is representative to compare the V-I and I-V operation regimes. See that identical results are found. It is important to note that the simulation

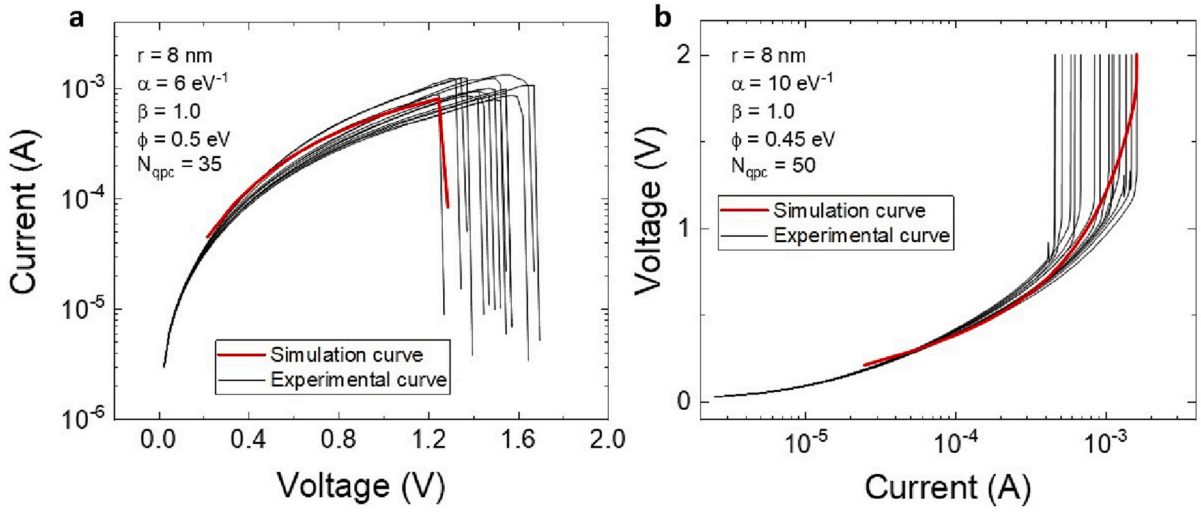

Fig. 9. Simulated (red lines) and experimental (black lines) curves for Ni/HfO_2/Si-n^+ devices. **a** I-V operation regime, **b** V-I operation regime. (For interpretation of the references to colour in this figure legend, the reader is referred to the web version of this article.)

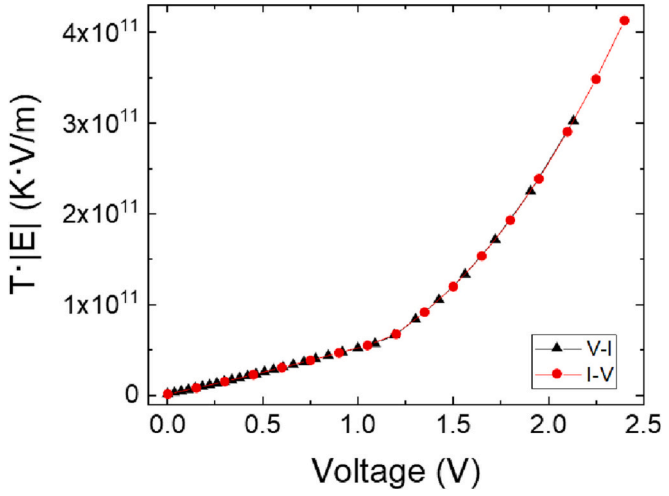

Fig. 10. Simulation of Ni/HfO_2/Si-n^+ devices; product of the temperature and the absolute value of the electric field versus the voltage value both for the I-V and V-I operation regimes.

approaches are different: when the voltage is fixed externally, this is easily transformed to boundary conditions in our simulation domain; however, if the current is fixed, we employ average probes to estimate the device voltage. We have also studied the output of current and voltage ramps, obtaining non-significative differences when making a fair comparison in terms of initial conditions (voltage and current magnitudes).

Considering the experimental results, it is clear that the V-I operation regime influences in a different way the physical processes behind RS. Consequently, a different modelling scheme is needed in this case (it might be related to modifications in Eq. 2, a reduction of the activation energy, or/and even linked to an increase of the heat generation term within the heat equation). Thus, the development of a new model would need of new experiments and indirect analysis of the experimental RS behaviour in our devices; in this respect, it is out the scope of this paper. As a general consideration, it is clear that the V-I regime influences RS operation, accelerating the physical mechanisms that create and destroy the CFs. These effects result in lower operation voltages (and power consumption) as well as lower variability. Therefore, it offers clear advantages for IC development in the non-volatile memories and neuromorphic computing realms.

In order to complete the simulation study and shed light on the resulting current/voltage signal in the RVS and RCS, respectively, we have used a different simulation approach based on a compact circuital model described in ref. [58]. This model was previously fitted and successfully used for studying reset transitions in Ni/HfO_2(20 nm)/Si-n^+ devices under different operation regimes (RVS and constant voltage stress) [58]. Fig. 11a shows the simulated I-V curve obtained under RVS (black line) and V-I under RCS (red lines) with the same slopes than the experimental input signals (0.4 V/s and 65 μA/s). The reset voltage and current are slightly lower under the RCS. When current and voltage are plotted versus time (insets in Fig. 11a), we can appreciate that the resulting signals are different under the RVS and RCS. However, if we simulate RCS with a higher slope (resulting in current and voltage signals closer to those obtained under RVS, green lines in Fig. 11a), the current and reset voltages are quite similar. As a conclusion, as happened with the previously exposed simulation approach based on a 3D finite elements solver, there is no difference between RVS and RCS, as long as the resulting current/voltage signals are similar.

Finally, Fig. 11b shows the simulated energy obtained by the time integration of the power. RCS with a lower slope leads to the highest total dissipated energy because the reset transition is delayed, even though the reset current/voltage are the lowest, this is consistent with the P_{reset} shown in Fig. 7a. RVS and RCS with higher slope produce quite similar dissipated energy, although current and voltage (and, therefore, energy) is slightly higher under RCS with 158 μA/s.

4. Conclusions

Carrying out the set and reset transitions applying current to RRAM HfO_2-based devices reduces set and reset voltages, as well as cycle-to-cycle variability in comparison with conventional voltage driven resistive switching operation. In addition, current controlled RS proves to be the most efficient method of carrying out the transitions between resistance states, as the power consumed is lower than voltage controlled resistive switching. This may be due to a better control of the Joule heating when applying current, as thermal effects are controlled by the device current. In addition, we have proven that, when employing conventional finite-element RRAM simulators, no apparent differences between I-V and V-I operation are obtained. Consequently, there is a need of further modelling in the case of V-I resistive switching since this regime influences in a different way the physical mechanisms behind the operation of the studied devices.

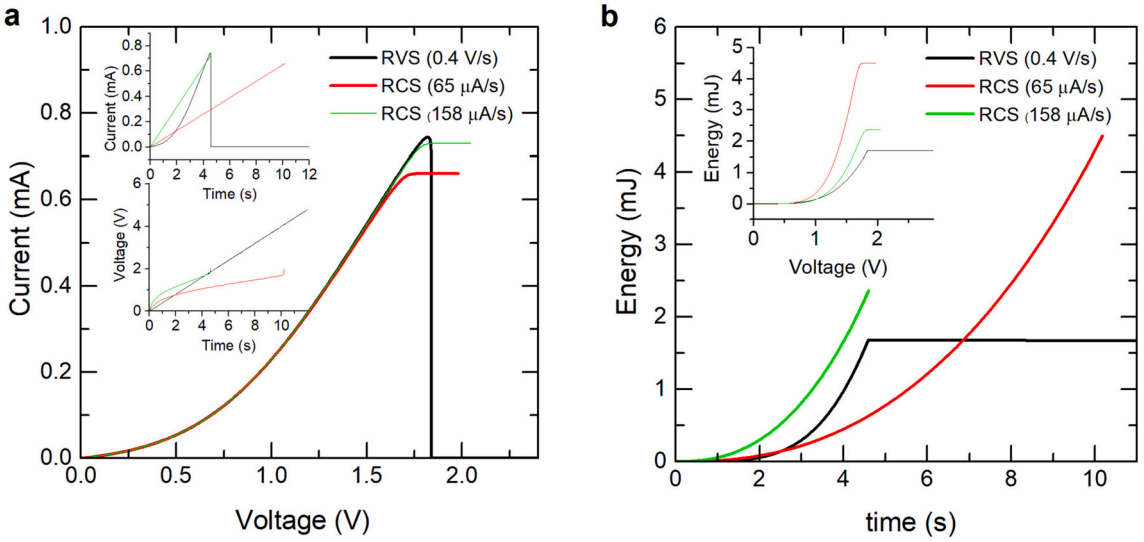

Fig. 11. **a** Simulated current versus device voltage under RVS (0.4 V/s), RCS (65 μA/s) and RCS (158 μA/s), (black, red and green lines, respectively) for the Ni/HfO_2/Si-n^+ devices. The signal slopes for the black and red lines are the same than those used in the experiments in this work. Insets: current and voltage signals versus time. **b** Simulated energy (calculated by the time integration of the dissipated power in the device) versus time for the same operation regimes than in **a**. **Inset**: energy versus resulting device voltage. (For interpretation of the references to colour in this figure legend, the reader is referred to the web version of this article.)

CRediT authorship contribution statement

G. Vinuesa: Investigation, Conceptualization, Methodology, Validation, Formal analysis, Writing – original draft, Visualization, Writing – review & editing. **H. García:** Investigation, Methodology, Validation, Software, Writing – review & editing. **J.M. Lendínez:** Investigation, Data curation. **E. García-Ochoa:** Data curation, Validation. **M.B. González:** Investigation, Resources, Funding acquisition, Writing – review & editing. **D. Maldonado:** Investigation, Data curation, Methodology, Software, Formal analysis, Writing – original draft. **C. Aguilera-Pedregosa:** Investigation, Data curation, Methodology, Software, Formal analysis, Writing – original draft. **E. Moreno:** Investigation, Data curation, Methodology, Software, Writing – original draft. **F. Jiménez-Molinos:** Investigation, Resources, Funding acquisition, Supervision, Project administration, Writing – review & editing. **J.B. Roldán:** Investigation, Resources, Funding acquisition, Supervision, Project administration. **F. Campabadal:** Resources, Funding acquisition, Project administration, Writing – review & editing. **H. Castán:** Resources, Funding acquisition, Supervision, Project administration, Writing – review & editing. **S. Dueñas:** Resources, Funding acquisition, Supervision, Project administration, Writing – review & editing.

Declaration of Competing Interest

The authors declare that they have no known competing financial interests or personal relationships that could have appeared to influence the work reported in this paper.

Data availability

Data will be made available on request.

Acknowledgments

The authors thank the support of the Consejería de Conocimiento, Investigación y Universidad, Junta de Andalucía (Spain) and the FEDER program for the project B-TIC-624-UGR20, as well as the Spanish Consejo Superior de Investigaciones Científicas (CSIC) for the intramural project 20225AT012. M.B. González acknowledges the Ramón y Cajal grant No. RYC2020-030150-I.

References

[1] M. Lanza, A. Sebastian, W.D. Lu, M. Le Gallo, M.-F. Chang, D. Akinwande, F. M. Puglisi, H.N. Alshareef, M. Liu, J.B. Roldan, Memristive technologies for data storage, computation, encryption and radio-frequency communication, Science 376 (6597) (2022) 1–13, https://doi.org/10.1126/science.abj9979, eabj9979.

[2] M. Lanza, H.-S.P. Wong, E. Pop, D. Ielmini, D. Strukov, B.C. Regan, L. Larcher, M. A. Villena, J.J. Yang, L. Goux, A. Belmonte, Y. Yang, F.M. Puglisi, J. Kang, B. Magyari-Köpe, E. Yalon, A. Kenyon, M. Buckwell, A. Mehonic, A. Shluger, H. Li, T.-H. Hou, B. Hudec, D. Akinwande, R. Ge, S. Ambrogio, J.B. Roldan, E. Miranda, J. Suñe, K.L. Pey, X. Wu, N. Raghavan, E. Wu, W.D. Lu, G. Navarro, W. Zhang, H. Wu, R. Li, A. Holleitner, U. Wurstbauer, M. Lemme, M. Liu, S. Long, Q. Liu, H. Lv, A. Padovani, P. Pavan, I. Valov, X. Jing, T. Han, K. Zhu, S. Chen, F. Hui, Y. Shi, Recommended methods to study resistive switching devices, Adv. Electron. Mater. 5 (2019) 1800143, https://doi.org/10.1002/aelm.201800143.

[3] A. Chen, Emerging research device roadmap and perspectives, in: 2014 IEEE International Conference on IC Design & Technology, Austin, TX, 2014, pp. 1–4, https://doi.org/10.1109/ICICDT.2014.6838616.

[4] Wm A. Wulf, S.A. McKee, Hitting the memory wall: implications of the obvious, SIGARCH Comput. Archit. News 23 (1) (1995) 20–24, https://doi.org/10.1145/216585.216588.

[5] H.-S. Philip Wong, H.-Y. Lee, S. Yu, Y.-S. Chen, Y. Wu, P.-S. Chen, B. Lee, F.T. Chen, M.-J. Tsai, Metal-Oxide RRAM, Proc. IEEE 100 (6) (2012) 1951–1970, https://doi.org/10.1109/JPROC.2012.2190369.

[6] V. Gupta, S. Kapur, S. Saurabh, A. Grover, Resistive random access memory: a review of device challenges, IETE Tech. Rev. 37 (4) (2020) 377–390, https://doi.org/10.1080/02564602.2019.1629341.

[7] A. Chen, A review of emerging non-volatile memory (NVM) technologies and applications, Solid State Electron. 125 (2016) 25–38, https://doi.org/10.1016/j.sse.2016.07.006.

[8] M. Lanza, R. Waser, D. Ielmini, J.J. Yang, L. Goux, J. Suñe, A.J. Kenyon, A. Mehonic, S. Spiga, V. Rana, S. Wiefels, S. Menzel, I. Valov, M.A. Villena, E. Miranda, X. Jing, F. Campabadal, M. Gonzalez, F. Aguirre, F. Palumbo, K. Zhu, J. B. Roldan, F.M. Puglisi, L. Larcher, T.-H. Hou, T. Prodromakis, Y. Yang, P. Huang, T. Wang, Y. Chai, K.L. Pey, N. Raghavan, S. Duenas, T. Wang, Q. Xia, S. Pazos, Standards for the characterization of endurance in resistive switching devices, ACS Nano 15 (11) (2021) 17214–17231, https://doi.org/10.1021/acsnano.1c06980.

[9] S. Spiga, A. Sebastian, D. Querlioz, B. Rajendran, Memristive Devices for Brain-Inspired Computing: From Materials, Devices, and Circuits to Applications-Computational Memory, Deep Learning, and Spiking Neural Networks, Woodhead Publishing Series in Electronic and Optical Materials, 2020, https://doi.org/10.1016/B978-0-08-102782-0.00025-3.

[10] R. Dittmann, S. Menzel, R. Waser, Nanoionic memristive phenomena in metal oxides: the valence change mechanisms, Adv. Phys. 70 (2021) 155–349, https://doi.org/10.1080/00018732.2022.2084006.

[11] S. Aldana, E. Pérez, F. Jimenez-Molinos, C. Wenger, J.B. Roldán, Kinetic Monte Carlo analysis of data retention in Al:HfO2-based resistive random access memories, Semicond. Sci. Technol. 35 (2020), 115012, https://doi.org/10.1088/1361-6641/abb072.

[12] C.-C. Chou, et al., An N40 256K×44 embedded RRAM macro with SL-precharge SA and low-voltage current limiter to improve read and write performance, in: Proc. IEEE Int. Solid-State Circuits Conf. (ISSCC), 2018, https://doi.org/10.1109/ISSCC.2018.8310392.

[13] C.-F. Yang, et al., Industrially applicable read disturb model and performance on mega-bit 28nm embedded RRAM, in: Proc. IEEE Symp. VLSI Technol., 2020, https://doi.org/10.1109/VLSITechnology18217.2020.9265060.
[14] C.-C. Chou, et al., A 22nm 96K×144 RRAM macro with a self-tracking reference and a low ripple charge pump to achieve a configurable read window and a wide operating voltage range, in: Proc. IEEE Symp. VLSI Circuits, 2020, https://doi.org/10.1109/VLSICircuits18222.2020.9163014.
[15] P. Jain, et al., A 3.6 Mb 10.1 Mb/mm2 embedded non-volatile Re-RAM macro in 22nm FinFET technology with adaptive forming/set/reset schemes yielding down to 0.5 V with sensing time of 5ns at 0.7 V, in: Proc. IEEE Int. Solid-State Circuits Conf. (ISSCC), 2019, https://doi.org/10.1109/ISSCC.2019.8662393.
[16] R. Khan, N. Ilyas, M.Z.M. Shamim, M.I. Khan, M. Sohail, N. Rahman, A.A. Khan, S. N. Khan, A. Khan, Oxide-based resistive switching-based devices: fabrication, influence parameters and applications, J. Mater. Chem. C 9 (44) (2021) 15755–15788, https://doi.org/10.1039/D1TC03420K.
[17] M. Nakayama, Reram technologies: applications and outlook, in: 2017 IEEE International Memory Workshop (IMW), Monterey, CA, USA, 2017, pp. 1–4, https://doi.org/10.1109/IMW.2017.7939099.
[18] A. Chen, Utilizing the variability of resistive random access memory to implement reconfigurable physical unclonable functions, IEEE Electron. Dev. Lett. 36 (2) (2015) 138–140, https://doi.org/10.1109/LED.2014.2385870.
[19] I. Chakraborty, A. Jaiswal, A.K. Saha, S.K. Gupta, K. Roy, Pathways to efficient neuromorphic computing with non-volatile memory technologies, Appl. Phys. Rev. 7 (2020), 021308, https://doi.org/10.1063/1.5113536.
[20] M. Hyung Jang, R. Agarwal, P. Nukala, D. Choi, A.T. Charlie Johnson, I.-W. Chen, R. Agarwal, Observing oxygen vacancy driven electroforming in Pt–TiO2–Pt device via strong metal support interaction, Nano Lett. 16 (4) (2016) 2139–2144, https://doi.org/10.1021/acs.nanolett.5b02951.
[21] F. Pan, S. Gao, C. Chen, C. Song, F. Zeng, Recent progress in resistive random access memories: materials, switching mechanisms and performance, Mater. Sci. Eng. 83 (2014) 1–59, https://doi.org/10.1016/j.mser.2014.06.002.
[22] M. von Witzleben, K. Fleck, C. Funck, B. Baumkötter, M. Zuric, A. Idt, T. Breuer, R. Waser, U. Böttger, S. Menzel, Investigation of the impact of high temperatures on the switching kinetics of redox-based resistive switching cells using a high-speed nanoheater, Adv. Electron. Mater. 3 (2017) 1700294, https://doi.org/10.1002/aelm.201700294.
[23] C. Giovinazzo, J. Sandrini, E. Shahrabi, O.T. Celik, Y. Leblebici, C. Ricciardi, Analog control of retainable resistance multistates in HfO2 resistive-switching random access memories (ReRAMs), ACS Appl. Electron. Mater. 1 (6) (2019) 900–909, https://doi.org/10.1021/acsaelm.9b00094.
[24] G. Bersuker, D.C. Gilmer, D. Veksler, Metal-oxide resistive random access memory (RRAM) technology: material and operation details and ramifications, in: Advances in Non-Volatile Memory and Storage Technology, Woodhead Publishing Series in Electronic and Optical Materials, 2019, pp. 35–102, https://doi.org/10.1016/B978-0-08-102584-0.00002-4.
[25] A.C. Jasmin, Filamentary model in resistive switching materials, in: AIP Conf. Proc. 1901, 2017, 060004, https://doi.org/10.1063/1.5010507.
[26] M.A. Villena, M.B. González, F. Jimenez-Molinos, F. Campabadal, J.B. Roldán, J. Suñé, E. Romera, E. Miranda, Simulation of thermal reset transitions in RRAMs including quantum effects, J. Appl. Phys. 115 (2014), 214504, https://doi.org/10.1063/1.4881500.
[27] S. Menzel, P. Kaupmann, R. Waser, Understanding filamentary growth in electrochemical metallization memory cells using kinetic Monte Carlo simulations, Nanoscale 7 (2015) 12673, https://doi.org/10.1039/C5NR02258D.
[28] K. Fujiwara, T. Nemoto, M.J. Rozenberg, Y. Nakamura, H. Takagi, Resistance switching and formation of a conductive bridge in metal/binary oxide/metal structure for memory devices, Jpn. J. Appl. Phys. 47 (2008) 6266, https://doi.org/10.1143/jjap.47.6266.
[29] X. Wu, S. Mei, M. Bosman, N. Raghavan, X. Zhang, D. Cha, K. Li, K. Leong Pey, Evolution of filament formation in Ni/HfO2/SiOx/Si-based RRAM devices, Adv. Electron. Mater. 1 (2015) 1500130, https://doi.org/10.1002/aelm.201500130.
[30] S. Claramunt, Q. Wu, M. Maestro, M. Porti, M.B. González, J. Martín-Martínez, F. Campabadal, M. Nafría, Non-homogeneous conduction of conductive filaments in Ni/HfO2/Si resistive switching structures observed with CAFM, Microelectron. Eng. 147 (2015) 335–338, https://doi.org/10.1016/j.mee.2015.04.112.
[31] C. Funck, S. Menzel, Comprehensive model of electron conduction in oxide-based memristive devices, ACS Appl. Electron. Mater. 3 (2021) 3674–3692, https://doi.org/10.1021/acsaelm.1c00398.
[32] S. Aldana, P. García-Fernández, R. Romero-Zaliz, M.B. González, F. Jiménez-Molinos, F. Gómez-Campos, F. Campabadal, J.B. Roldán, Resistive switching in HfO2 based valence change memories, a comprehensive 3D kinetic Monte Carlo approach, J. Phys. D. Appl. Phys. 53 (2020), 225106, https://doi.org/10.1088/1361-6463/ab7bb6.
[33] S. Aldana, P. García-Fernández, A. Rodríguez-Fernández, R. Romero-Zaliz, M. B. González, F. Jiménez-Molinos, F. Campabadal, F. Gómez-Campos, J.B. Roldán, A 3D kinetic Monte Carlo simulation study of resistive switching processes in Ni/HfO2/Si-n+−based RRAMs, J. Phys. D. Appl. Phys. 50 (2017), 335103, https://doi.org/10.1088/1361-6463/aa7939.
[34] J.B. Roldán, G. González-Cordero, R. Picos, E. Miranda, F. Palumbo, F. Jiménez-Molinos, E. Moreno, D. Maldonado, S.B. Baldomá, M. Moner Al Chawa, C. de Benito, S.G. Stavrinides, J. Suñé, L.O. Chua, On the thermal models for resistive random access memory circuit simulation, Nanomaterials 11 (2021) 1261, https://doi.org/10.3390/nano11051261.
[35] R. Waser, Redox-based resistive switching memories, J. Nanosci. Nanotechnol. 12 (10) (2012) 7628–7640, https://doi.org/10.1166/jnn.2012.6652.
[36] I. Valov, Redox-based resistive switching memories (ReRAMs): electrochemical systems at the atomic scale, ChemElectroChem 1 (2014) 26–36, https://doi.org/10.1002/celc.201300165.
[37] D. Ielmini, R. Bruchhaus, R. Waser, Thermochemical resistive switching: materials, mechanisms, and scaling projections, Phase Transit. 84 (7) (2011) 570–602, https://doi.org/10.1080/01411594.2011.561478.
[38] S.H. Chang, J.S. Lee, S.C. Chae, S.B. Lee, C. Liu, B. Kahng, D.-W. Kim, T.W. Noh, Occurrence of both unipolar memory and threshold resistance switching in a NiO film, Phys. Rev. Lett. 102 (2009), 026801, https://doi.org/10.1103/PhysRevLett.102.026801.
[39] L. Goux, S. Spiga, Unipolar resistive-switching mechanisms, in: Resistive Switching: From Fundamentals of Nanoionic Redox Processes to Memristive Device Applications, 2016, pp. 363–394, https://doi.org/10.1002/9783527680870.ch13.
[40] H. Sun, Q. Liu, S. Long, H. Lv, W. Banerjee, M. Liu, Multilevel unipolar resistive switching with negative differential resistance effect in Ag/SiO2/Pt device, J. Appl. Phys. 116 (2014), 154509, https://doi.org/10.1063/1.4898807.
[41] W. Hu, X. Chen, G. Wu, Y. Lin, N. Qin, D. Bao, Bipolar and tri-state unipolar resistive switching behaviors in Ag/ZnFe2O4/Pt memory devices, Appl. Phys. Lett. 101 (2012), 063501, https://doi.org/10.1063/1.4744950.
[42] W. Wang, B. Zhang, H. Zhao, Forming-free bipolar and unipolar resistive switching behaviors with low operating voltage in Ag/Ti/CeO2/Pt devices, Results Phys. 16 (2020), 103001, https://doi.org/10.1016/j.rinp.2020.103001.
[43] X. Wu, D. Cha, M. Bosman, N. Raghavan, D.B. Migas, V.E. Borisenko, X.-X. Zhang, K. Li, K.-L. Pey, Intrinsic nanofilamentation in resistive switching, J. Appl. Phys. 113 (2013), 114503, https://doi.org/10.1063/1.4794519.
[44] K.-L. Lin, T.-H. Hou, J. Shieh, J.-H. Lin, C.-T. Chou, Y.-J. Lee, Electrode dependence of filament formation in HfO2 resistive-switching memory, J. Appl. Phys. 109 (2011), 084104, https://doi.org/10.1063/1.3567915.
[45] A. Rodriguez, M.B. Gonzalez, E. Miranda, F. Campabadal, J. Suñe, Temperature and polarity dependence of the switching behavior of Ni/HfO2-based RRAM devices, Microelectron. Eng. 147 (2015) 75–78, https://doi.org/10.1016/j.mee.2015.04.038.
[46] M.A. Villena, M.B. González, J.B. Roldán, F. Campabadal, F. Jiménez-Molinos, F. M. Gómez-Campos, J. Suñé, An in-depth study of thermal effects in reset transitions in HfO2 based RRAMs, Solid State Electron. 111 (2015) 47–51, https://doi.org/10.1016/j.sse.2015.04.008.
[47] Y. Chen, ReRAM: history, status, and future, IEEE Trans. Electron. Dev. 67 (4) (2020) 1420–1433, https://doi.org/10.1109/TED.2019.2961505.
[48] D. Ielmini, Resistive switching memories based on metal oxides: mechanisms, reliability and scaling, Semicond. Sci. Technol. 31 (6) (2016), 063002, https://doi.org/10.1088/0268-1242/31/6/063002.
[49] H. García, S. Dueñas, Ó.G. Ossorio, H. Castán, Current pulses to control the conductance in RRAM devices, IEEE J. Electron Devices Soc. 8 (2020) 291–296, https://doi.org/10.1109/JEDS.2020.2979293.
[50] H. García, Ó.G. Ossorio, S. Dueñas, H. Castán, Current and voltage control of intermediate states in bipolar Rram devices for Neuristor applications, ECS Trans. 97 (1) (2020) 17, https://doi.org/10.1149/09701.0017ecst.
[51] M. Maestro, M.B. González, F. Jiménez-Molinos, E. Moreno, J.B. Roldán, F. Campabadal, Unipolar resistive switching behavior in Al2O3/HfO2 multilayer dielectric stacks: fabrication, characterization and simulation, Nanotechnology 31 (2020), 135202, https://doi.org/10.1088/1361-6528/ab5f9a.
[52] G. Martín, M.B. González, F. Campabadal, F. Peiró, A. Cornet, S. Estradé, Transmission electron microscopy assessment of conductive-filament formation in Ni–HfO2–Si resistive-switching operational devices, Appl. Phys. Express 11 (2018), 014101, https://doi.org/10.7567/APEX.11.014101.
[53] D. Maldonado, S. Aldana, M.B. González, F. Jiménez-Molinos, F. Campabadal, J. B. Roldán, Parameter extraction techniques for the analysis and modeling of resistive memories, Microelectron. Eng. 265 (2022), 111876, https://doi.org/10.1016/j.mee.2022.111876.
[54] E. Miranda, J. Suñé, Analytic modeling of leakage current through multiple breakdown paths in SiO2 films, in: IEEE International Reliability Physics Symposium Proceedings, 2001-January, 2001, pp. 367–379, https://doi.org/10.1109/RELPHY.2001.922929.
[55] L.M. Prócel, L. Trojman, J. Moreno, F. Crupi, V. Maccaronio, R. Degraeve, L. Goux, E. Simoen, Experimental evidence of the quantum point contact theory in the conduction mechanism of bipolar HfO2-based resistive random access memories, J. Appl. Phys. 114 (2013) 7, https://doi.org/10.1063/1.4818499.
[56] J.B. Roldán, E. Miranda, G. González-Cordero, P. García-Fernández, R. Romero-Zaliz, P. González-Rodelas, A.M. Aguilera, M.B. González, F. Jiménez-Molinos, Multivariate analysis and extraction of parameters in resistive RAMs using the Quantum Point Contact model, J. Appl. Phys. 123 (2018), 014501, https://doi.org/10.1063/1.5006995.
[57] D. Ielmini, Modeling the universal set/reset characteristics of bipolar RRAM by field- and temperature-driven filament growth, IEEE Trans. Electron. Dev. 58 (2011) 4309–4317, https://doi.org/10.1109/TED.2011.2167513.
[58] G. González-Cordero, F. Jiménez-Molinos, J.B. Roldán, M.B. González, F. Campabadal, Transient Spice simulation of Ni/HfO_2/Si-n^+ resistive memories, published in 2016 Conference on Design of Circuits and Integrated Systems (DCIS), 2022, https://doi.org/10.1109/DCIS.2016.7845384.